Journal of Electroanalytical Chemistry 976 (2025) 118807

Contents lists available at ScienceDirect

Journal of Electroanalytical Chemistry

journal homepage: www.elsevier.com/locate/jelechem

Synergistic electrochemical performance of $NdFeO_3$/rGO composite for enhanced oxygen and hydrogen evolution reactions

Khalid A. Alrashidi [a], Iram Manzoor [b], Abdul Ghafoor Abid [c], Saikh Mohammad [a], Muhammad Bilal [d], Nadir Abbas [e], Farooq Ahmad [f], Jafar Hussain Shah [g,*]

[a] Department of Chemistry, College of Science, King Saud University, Riyadh 11451, Saudi Arabia
[b] Department of Physics, the Islamia University of Bahawalpur, 63100, Pakistan
[c] State key Laboratory of Structural Chemistry, Fujin Institute of Research on the Structure of Matter, Chainese Academy of Sciences (CAS), Fuzhou 350002 Fujin, China
[d] Centre of Excellence in Solid State Physics University of the Punjab Lahore Pakistan
[e] School of Geography, Geology and the Environment, University of Leicester, Leicester, United Kingdom
[f] Institute of Molecular Physics Polish Academy of Sciences Poznan Poland
[g] Institute of Fundamental and Frontier Sciences, University of Electronic Science and Technology of China, Chengdu, Sichuan, China

ARTICLE INFO

Keywords:
$NdFeO_3$/rGO
Composite
OER
HER
Charge transfer kinetics

ABSTRACT

The research delves into a comprehensive process for synthesizing and characterizing $NdFeO_3$, reduced graphene oxide (rGO), and their composite. In present work, the $NdFeO_3$/rGO composite is synthesized using ultrasonic methods. Subsequently, techniques such as FT-IR, XRD, SEM, EDX, and XPS univocally affirmed the synthesis of $NdFeO_3$/rGO. The pristine materials $NdFeO_3$, rGO, and $NdFeO_3$/rGO were investigated for oxygen evolution reaction (OER) and hydrogen evolution reaction. The findings reveal that the $NdFeO_3$/rGO composite exhibits superior OER and HER compared to individual components in the presence of 1 M KOH solution. The $NdFeO_3$/rGO at current densities of 100, 500 and 1000 $mAcm^{-2}$ displays lower overpotentials 220, 255 and 345 mV for OER and enhanced stability over extended testing periods for 80 h. Similarly, composite at current densities of 100, 500, and 1000 $mAcm^{-2}$ to acquire overpotentials of 206, 301, and 466 mV, respectively. The exalted electrocatalytic performance of $NdFeO_3$/rGO is related to the production of synergism between $NdFeO_3$ and rGO, promoting faster charge transfer kinetics and catalytic activity. Overall, the study underscores the potential of $NdFeO_3$/rGO as promising and inexpensive electrocatalysts for OER and HER, offering significant promise for applications in sustainable energy conversion.

1. Introduction

Each country pursues alternative energy sources as a means to maintain technological progress and boost the economy. Existing scientific research is oriented toward the ultimate goal of life on earth. The overarching goal of modern science is to create an inexhaustible and long-lasting energy source capable of supporting life on our planet. The significance of fossil fuels has diminished due to their depletion and the emission of harmful substances when they are burned in power plants and vehicles, so hydrogen is the clean energy source [1]. The scientific community prioritized alternative unconventional energy sources over conventionally hazardous fossil fuels due to these factors. Attempts to generate energy from sources such as solar, air batteries, hydrodynamic, and water splitting have been unsuccessful. Numerous studies examining contemporary fuels have demonstrated that hydrogen (H_2) exhibits superior performance in terms of efficiency and accessibility when assessed as a sustainable substitute fuel [2]. A variety of methods were explored for the production of H_2; nevertheless, the most dynamic and advantageous H_2 was generated via water electrocatalysis and photocatalysis [3,4]. The scientific community is concerned about electrocatalytic water splitting in light of the energy crisis, which is characterized by alarming environmental contamination, calamitous energy conditions, and an economy that is similarly devastated. Both the HER and OER are produced at the cell's cathode and anode via dynamic water splitting [5–8]. OER, which is the sluggish reaction has been the subject of extensive research [9]. It impacts the overall process efficiency due to the lethargic kinetics it exhibits [10]. To produce products, reactants must typically surmount an energetic gradient, also known as

* Corresponding author.
E-mail address: jafarhussain@uestc.edu.cn (J.H. Shah).

https://doi.org/10.1016/j.jelechem.2024.118807
Received 2 September 2024; Received in revised form 11 November 2024; Accepted 13 November 2024
Available online 16 November 2024

the energy of activation. To accomplish the reaction, the four-electron transfer mechanism of OER must ascend a substantial energy peak known as the activated complex. The efficiency of electrochemical water splitting is enhanced in acidic solid environments, whereas severe conditions are required for this process. In order to optimize the performance of the reaction and guarantee its economic viability, it is necessary to develop a catalyst that modifies the trajectory of the reaction while requiring the least amount of activation energy. To facilitate a chemical reaction, it is necessary for intermediates to bind to the surface of the electrocatalyst. An electrocatalyst has to be inexpensive and have a greater surface area in order to be considered optimal for the adsorption of reaction intermediates. It should also be more electrochemically active. Additionally, it ought to facilitate the desorption of molecules, a crucial step in the creation of the finished goods.

Recently, the perovskites and spinals have attained a lot of attention owing to their potential to carry out electrocatalysis in energy conversion and storage devices [11]. Particularly for the water splitting reactions such as OER and HER [12].The structure of perovskites mainly consists of two type of cations occupying A-site mostly rare earth metals reside at this site and alkaline earth metals occupy B-site. Owing to presence of carious cation sites, these oxides have been regarded as most diverse structures and display versatile properties [13,14].The distinctive crystal structure of perovskite oxides enables easy redox reactions and numerous active sites, making them extremely sought-after for electrocatalytic applications. In addition, their remarkable stability and ability to function effectively in water-based environments make them excellent choices for extended use in electrochemical devices [15,16]. Exploring novel materials to further boost OER and HER in alkaline media is crucial, as these reactions are critical for numerous energy conversion and storage devices [17,18]. The unique morphology and lattice structure of nanomaterials have been considered important to synthesize a novel electrocatalyst. Over the last twenty years, there has been considerable attention directed towards the synthesis and analysis of nanoparticles and nanostructured materials spanning diverse chemical compositions, structures, and morphologies. In this regard, the orthoferrite such as neodymium iron oxide have not been explored for the electrocatalysis of water molecules. It is a distorted structure arrange orthorhombically comprising diverse potential for the vast spectrum of energy devices. The unit cell of $NdFeO_3$ retains Nd^{3+} ions occupying the A site and Fe^{3+} ions residing at the B site [19,20].In addition, $NdFeO_3$ displays intriguing magnetic and electronic properties, indicating its potential for use in electrocatalytic applications. $NdFeO_3$ shows great potential as an electrocatalyst for both the OER and HER, which are important steps in the overall process of water splitting. However, there has been a lot of work done on the various properties of properties of $NdFeO_3$ such as electronic and magnetic features, but no work is done for the OER and HER [21,22].

Nanostructured materials of $NdFeO_3$ have been synthesized using a variety of approaches, including methods involving gas-phase, liquid-phase, and mixed-phase techniques. Notably, ultrasound has emerged as a prominent method explored for its synthesis [17,23]. Sono-chemical procedures that use ultrasound provide advantages such as homogeneous nucleation and significantly quicker crystallization than typical heating methods, allowing for the development of nanostructured materials. Ultrasound causes physical and chemical effects through sonic cavitation, resulting in intense circumstances of high pressures, temperatures, and rapid molecular motion. These circumstances cause bond breakdown, the generation of free radicals, mechanical shocks, and strong shear gradients, allowing access to previously inaccessible reaction areas and promoting the development of nanostructured and tailored material [24].

Furthermore, reduced graphene oxide (rGO) is cherished for energy conversion and storage technologies, particularly in electrocatalytic water splitting reactions. Its notable features include outstanding electrical conductivity, stemming from the restoration of the sp^2 carbon network during reduction processes [15,25–27]. Generally, graphene oxide (GO) comprises a single atomic layer of functionalized graphene. GO demonstrates immense structural and electrical features attributed to edge/basal plane sites and the oxygenated species, which are expected to contribute substantially to cyclic voltammetry. Additionally, GO plays a crucial role in other allied fields, including fabricating energy storage devices, implementing them as membrane materials, and monitoring nucleic acid, ascorbic acid, dopamine, and uric acid levels [28,29]. Furthermore, when integrated with other catalytic materials or nanoparticles, rGO can evoke synergistic effects that further enhance its catalytic prowess. Importantly. Its cheapness and facile synthesis route by utilizing earth abundant and economical precursors made it a sought-after option for industrial and practical applications [30,31].

In this work, we developed a straightforward strategy for manufacturing $NdFeO_3$ at low temperatures using ultrasonic waves in an ultrasonic bath. Later, the nanoparticles were dispersed and physically combine with the rGO nanosheets. In this method, the surfactant octanoic acid is used to avoid agglomeration and control the nucleation process which led towards the preparation of small, uniformly distributed nanoparticles. When the precursor is heated to 600 °C, it turns into solid nanoparticles with a perovskite structure. This method claims to have faster reaction times and does not need high temperatures like other methods. Also, smaller particles are made when ultrasound energy is present. The results of the $NdFeO_3$/rGO composite subjected to an electrochemical examination in a 1 M KOH solution showed that it outperforms the individual $NdFeO_3$ and rGO in OER and HER. OER has shown remarkable activity augmented by current densities of 100, 500, and 1000 $mAcm^{-2}$ at lower overpotentials of 220, 255, and 345 mV, respectively. Additionally, it demonstrates improved stability over long testing periods, surpassing 80 h. Similarly, the hydrogen evolution process obtained higher current densities of 100, 500, and 1000 $mAcm^{-2}$ at lower overpotentials of 206, 301, and 466 mV, respectively. This excellent performance is garnered by increased electrochemically active surface area and unusual shape provided by the unique combination of the NdFeO3/rGO composite structure.

2. Experimental section

2.1. Materials and Reagents

Neodymium chloride hexahydrate (98 % purity) and iron chloride hexahydrate $FeCl_3{\cdot}6H_2O$ (99 % purity), NaOH pellets (97 % purity), potassium permanganate (99 % purity), and graphite powder were acquired from Sigma-Aldrich. Additionally, deionized water was used throughout the process.

2.2. Synthesis of neodymium iron oxide

To prepare $NdFeO_3$ nanoparticles, 0.1 M of $FeCl_3{\cdot}6H_2O$ and 0.1 M $NdCl_3{\cdot}6H_2O$ dissolved in a 50 ml deionized water. To this combination, 2 ml of octanoic acid was added as a surfactant and coating ingredient. Then, a 1.5 M NaOH solution was gradually transferred until pH of the combination reached 7–8, resulting in full precipitation. The resultant liquid precipitate was irradiated with ultrasonic vibrations. After the mixture had cooled to room temperature, and centrifuged for 15 min at 3000 rpm to separate precipitates. The precipitates were subsequently whisked multiple times with deionized water and ethanol to purge any surplus surfactant. Following the washing operations, the precipitate was heated in an oven at 90 °C for 4 h to eliminate any remaining moisture. Finally, the resultant lightweight powder was calcined at 600 °C for 4 h to remove any leftover organic residues. Sonication was shown to be effective in facilitating the development of nanoparticles' crystalline phase. In the experimental circumstances specified, sonication for 20 min at 65 °C produced the purest $NdFeO_3$ phase.

2.3. Preparation of reduced graphene oxide

To prepare reduced graphene oxide (rGO), initially the graphene oxide has been synthesized utilizing the graphite flakes (0.1 g), and adding the required amount of potassium permanganate as oxidizing agent. The oxidation of graphite incorporates oxygen bearing functional groups into GO sheets. It makes it more hydrophilic and disperse in water easily. Later, GO is exfoliated through sonication into Graphene oxide sheets separately. The resulting GO is then exfoliated to separate individual sheets, through sonication and dispersed in a 100 ml DMF as a solvent. Reduction of GO is then carried out to remove or reduce the oxygen functional groups, restoring some of the sp^2 hybridized carbon structure characteristic of graphene. Chemical reduction using agents like hydrazine through annealing at 200 °C temperature. Through this reduction process, the electrical conductivity of the material is improved. The synthesized rGO is subsequently washed to remove any residual chemicals and heated in oven for a day at 60 °C to ensure stability.

2.4. Preparation of composite $NdFeO_3$/rGO

To prepare the composite $NdFeO_3$/rGO, the precursor solution of $NdFeO_3$ is prepared by following the above-mentioned procedure. The prepared rGO is added to the $NdFeO_3$ precursor solution and after that the ultrasonic irritation is carried out to deposit the nanoparticles of $NdFeO_3$ on to the nanosheets of rGO. Following the product is cleaned with C_2H_5OH and DI H_2O and separated via ultracentrifugation. The obtained powder was dried in the oven at 90°C for 4 h. Finally, the resultant was calcined at 200 °C for 2 h to procure $NdFeO_3$/rGO. The whole process for the fabrication of was $NdFeO_3$/rGO is displayed in scheme 1.

2.5. Physical characterization

The ultrasonic irradiation was carried out using an ultrasonic instrument (Ultrasonic Tech Elite) Equipped with a high-performance titanium oscillator (horn) and a powerful multi-wave ultrasonic generator. Using the KBr disk approach, FT-IR spectra were obtained using a NanoSpecPlus spectrophotometer in the 500–4000 cm^{-1} range. Introducing the XRD Analytica 5000, a 20-graphite monochromatic Cu Kα X-ray source, this instrument ensures exceptional sensitivity and resolution, was leveraged to conduct the X-ray powder diffraction (XRD) investigation at room temperature in the 60 range. The images were captured using an energy dispersive X-ray (EDX) microanalysis system integrated into a scanning electron microscope (Hileos). For X-ray photoelectron spectroscopy (XPS), a common instrument model is the "Thermo Scientific ESCALAB Xi is used.

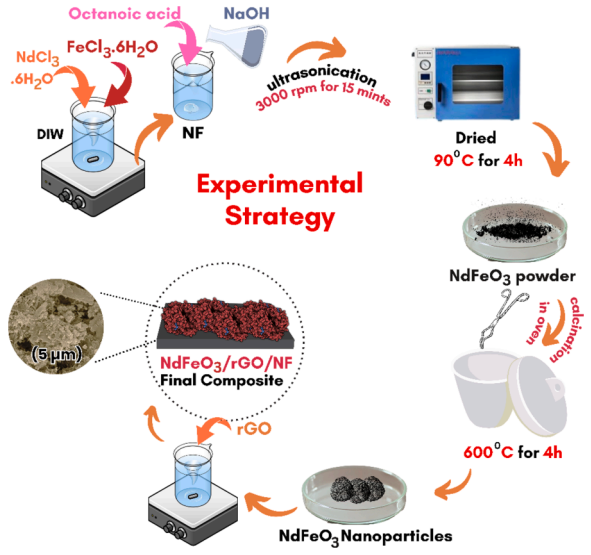

Scheme 1. Fabrication of $NdFeO_3$/rGO nanoparticles via ultrasonication method.

2.6. Preparation of ink

First, take a clean small beaker and carefully measure out 7 mg of catalyst. Next, to improve the catalyst's adhesion the electrode surface was modified by adding 7 µL of Nafion solution (5 % w/v in alcohol) to the mixture. The ink is evenly distributed by sonicating it in a sonicator for 30 min. The coating of NF is done by using micropipette (3 µL of ink) and let it dry in an oven to make a thin layer of ink catalyst.

2.7. Electrochemical tests

A computerized Auto Lab potentiostat (PGSTAT-204) was leveraged for various electrochemical investigations. Those involve polarization curve (CV), controlled potential bulk electrolysis (CPE), linear sweep voltammetry (LSV), and impedance spectroscopy (EIS). The working electrodes, a platinum wire counter electrode, and an Ag/AgCl (3.0 M KCl) reference electrode immersed in the electrolyte-containing Teflon-lined Pyrex glass vessel. The electrochemical cell was cleaned using a 3:1 volumetric solution of HNO_3 and H_2SO_4 boiled in deionized water before use. Furthermore, it was then also rinsed with acetone. Similarly, the counter electrode was immersed in 20 % HNO_3 for 15 min and then washed with deionized water. All equipment was heated for 40 min in an oven warmed at 353.15 K. Afterwards, commercially available spinning disk electrodes were washed with acetone and deionized water before being used as functional electrodes. All processes were performed out in 1.0 M KOH solution at 298.15 K and 13.5 pH. CV measurements were conducted by purposefully cycling between negative and positive potentials at a scanning rate of 10 mVs^{-1}. The electrode's geometric surface area was included into all current measurements. To guarantee accuracy and reproducibility, experiments were repeated using data that was collected at room temperature. The geometric surface area of the working electrode (0.5 cm^2) was used to calculate each current density (j). Equation (1) was then used to convert the potential of the Ag/AgCl reference electrode to that of the Reversible Hydrogen Electrode [32]

$$E_{RHE} = E_{Ag/AgCl} + E + 0.059 \times pH \quad (1)$$

whereas the symbol E represents the standard potential for a 3.0 M KCl solution containing a silver wire; 0.197 and 0.059 are the correction factors. The relation provided applies to IR compensation [33].

$$E_{actual} = E_{experimental} - IR \quad (2)$$

The catalytic and kinetic activity of the electrocatalysts was measured using Tafel plots generated by CV. The technique was to create steady-state polarization curve in a linear range and then use Equation (3) to assess its effectiveness [34].

$$\eta = a + (2.303 \times R \times T/\alpha nF) \times logj \quad (3)$$

To calculate the slope, average the quantities of e-1 exchanged throughout redox reactions (n = e-1), F = 96,485 (Faraday constant), j = current density, and η = overpotential in mV. The slope is represented as 2.303/F. polarization curves in the non-Faradic potential range of 10–60 mVs^{-1} at different scanning speeds. To calculate the electrochemical active surface area (ECSA), divide the obtained double layer capacitance (C_{dl}) by the specific capacitance of the previously reported planar electrodes (0.04 Fcm^{-2}). Equations (4) and (5) were utilized to determine the ECSA [35,36].

$$C_{dl} = \frac{Slope}{2} \quad (4)$$

$$ECSA = \frac{C_{dl}}{C_{sp}} \quad (5)$$

The charge transfer resistance (Rct) and solution resistance (Rs) of a 1.0 M alkaline solution were measured using electrochemical impedance spectroscopy (EIS). The technique included measuring the semicircle diameter of the Nyquist plot between 0.1 and 100,000 Hz, with an amplitude of 5.0 mV. Besides, Randle circuit model was used to get the values of Rct and Rs [37].

3. Results and Discussion

3.1. Structural, morphological and compositional analysis

The X-ray diffraction (XRD) pattern shown in Fig. 1 provides strong proof that $NdFeO_3$ nanoparticles were successfully synthesized. According to JCPDS File no. 01–074-1473, the analysis solely shows diffraction peaks that correspond to the perovskite-type $NdFeO_3$ phase. The crystal structure of $NdFeO_3$ is orthorhombic, and a diffraction peak at d = 3.879 Å indicates the (112) plane. The existence of indexed Miller indices provides additional evidence that $NdFeO_3$ nanoparticles have been formed. The fact that there are no peaks corresponding to Nd_2O_3 or Fe_2O_3 shows that the precursor compounds have been fully transformed into a single $NdFeO_3$ phase. Peak sharpening indicates enhanced nanoparticle crystallinity, and peak absence corresponding to impurities highlights the cleanliness of the produced $NdFeO_3$. The development of smaller $NdFeO_3$ nanoparticles is confirmed by the broadening of the peaks, which in turn indicates the particles' nanometer-scale dimensions. The unit cell structure of $NdFeO_3$ adheres to the classic perovskite crystal lattice, characterized by the arrangement of Nd^{3+} and Fe^{3+} ions surrounded by oxygen ions. Within this structure, Nd^{3+} ions occupy the A-site, featuring a coordination number of 12 and forming interactions with neighboring oxygen ions. Similarly, Fe^{3+} ions reside in the B-site of the lattice, also exhibiting a coordination number of 12 and surrounded by oxygen ions forming octahedral coordination geometries. The corner of octahedral is shared by oxygen ions making interconnected layers of Nd and Fe ions elongate across the whole unit cell structure. This type of structure showcases the distinct features of perovskite depicting the cubic symmetry making it unique for catalyzing the electrochemical reactions. This cubic symmetry distorted when form composite with rGO owing to the alteration occurred in the electronic structure of $NdFeO_3$. This change is estimated by tolerance factor (discussed later) and measuring the lattice parameters of obtained XRD pattern. The XRD analysis for the reduced graphene oxide shows the broad peaks which correspond to the conjugated carbon network. It shows a prominent peak around 2θ = 24.5', indicating the graphitic carbon planes which is connected via conjugated Π=Π bond. The broadening of peak can be ascribed to the interlayer defects, disordered structure and reduced crystallinity. On the other hand, the XRD pattern for the composite showcasing the diffraction peaks for both nanoparticles of $NdFeO_3$ and rGO. It typically exhibits peaks for the $NdFeO_3$ and a peak at 2θ = 24.5reflect that the nanoparticles of $NdFeO_3$ are uniformly attached to the surface of rGO. The comparison of lattice constant and cell volume is shown in Table 1.. Overall, XRD analysis of $NdFeO_3$/rGO composites aids in understanding their structural properties, phase composition, and potential applications across various fields.

In order to estimate the lattice constant and cell volume of $NdFeO_3$ and $NdFeO_3$/rGO using Bragg equation. The brags law led to understand the structure of interconnected layers of $NdFeO_3$ and $NdFeO_3$/rGO. For it, the d-spacing is calculated using the following equation.

Table 1
Lattice parameters, Cell volume and average size calculated by using lattice constant equations and Scherer formula for $NdFeO_3$ and $NdFeO_3$/rGO.

Sample	Lattice constant(Å)			Cell volume V (Å)	Average size (nm)
$NdFeO_2$	a	b	c	235.67	33 ± 1
	5.56	7.7	5.4		
$NdFeO_2$/rGO	5.6	8.8	5.4	266.11	30 ± 1

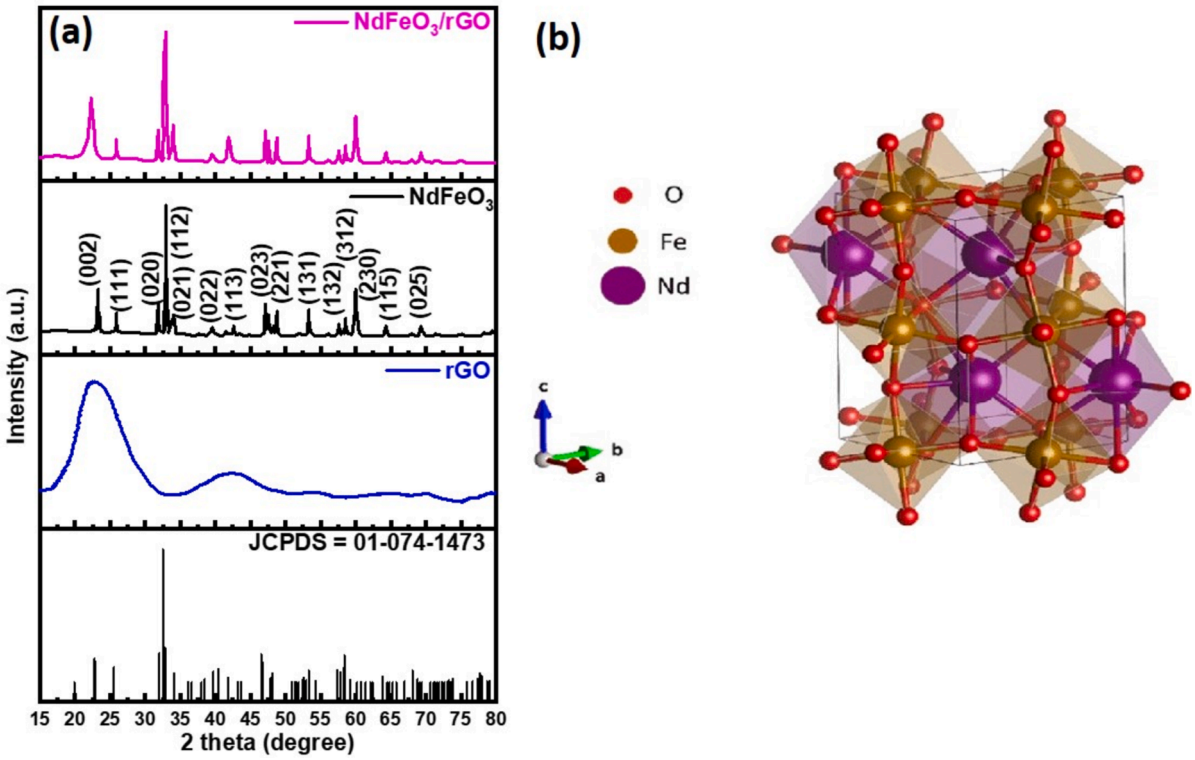

Fig. 1. (a) Comparison of XRD pattern for $NdFeO_3$, rGO and $NdFeO_3$/rGO, and (b) Unit cell structure for $NdFeO_3$.

$$1/d2 = h2/a2 + k2/b2 + l2/c2 \quad (6)$$

For cubic system, the cell volume is calculated by using the given equation:

$$V = a.b.c \quad (7)$$

Crystallite size (D) can be evaluated using the Scherrer equation:

$$Dc = K\lambda/\beta cos\theta \quad (8)$$

Here, D = the average crystallite size, K = the shape factor (commonly taken as 0.9), λ = the wavelength of X-ray radiation, B = the full width at half maximum (FWHM) of the peak, θ = the Bragg angle [38]

Fig. 2 depicts the comparison of FT-IR spectra for the product post-calcination, spanning frequencies within 4000 to 500 cm^{-1}. FTIR spectroscopy serves as a valuable tool for scrutinizing the functional groups and bonds in the materials. In the analysis of $NdFeO_3$, rGO, and $NdFeO_3$/ rGO, FTIR analysis typically reveals the characteristic absorption peaks corresponding to the stretching and bending vibrations of metal–oxygen bonds in the perovskite structure. These peaks are usually observed in the infrared region, with prominent bands at specific wave numbers corresponding to the vibrational modes of the Nd-O and Fe-O bonds. The metal–oxygen bond usually generate stretching vibrations at the wave number of 567 cm^{-1}, 599 cm^{-1} [38] respectively and the bands at 650 cm^{-1} correspond to the bending vibrations [38,39]. The most common vibrations in rGO, are produced correspond to the functional groups such as hydroxyl, carboxyl and carbonyl groups. The characteristics peak at 3700 cm^{-1} [25] correspond to the hydroxyl group.. Similarly, carbonyl groups around 1750 cm^{-1} [40] and carboxyl groups around 1650 cm^{-1} in the rGO nanosheets. The FTIR spectra for the $NdFeO_3$/rGO, composed of characteristics peaks for both $NdFeO_3$ and rGO. According to the spectra, the peaks at 567 cm^{-1} and 678 cm^{-1} correspond to the presence of Nd-O and Fe-O bonds. While the characteristics peaks for rGO are present at 1750, 165, and 3700 cm^{-1} confirming the presence of functional groups carboxyl, carbonyl and hydroxyl groups in the crystal structure of composite $NdFeO_3$/rGO. This finding proves the formation of the perovskite $NdFeO_3$ and is in accordance with the XRD data.

The morphological characterization is done by using the SEM technique. The exfoliated nanosheets of rGO is depicted in Fig. 2b. SEM analysis revealed thickness of rGO is around 14 nm. Moreover, the rough surface and stacked layers of rGO are beneficial for the catalysis properties. Similarly, the Fig. 2c depicts the nanorods of $NdFeO_3$. The nanorods are small in size and evenly distributed having thickness of 2 nm and average particle size of around 33 nm having spherical shape estimated by SEM analysis.

The SEM analysis for the composite material depicts the uniform dispersion of nanorods of $NdFeO_3$ onto surface of rGO shown in Fig. 3a. These results shows the fabricated material has good porocity with good mechanical and all other properties [41]. The internal morphology is assessed via using the TEM technique. TEM images of $NdFeO_3$, rGO and $NdFeO_3$/rGO are presented in Fig. 3b. The TEM analysis exhibiting the formation of small nanorods having 1 nm of thickness entangled inside

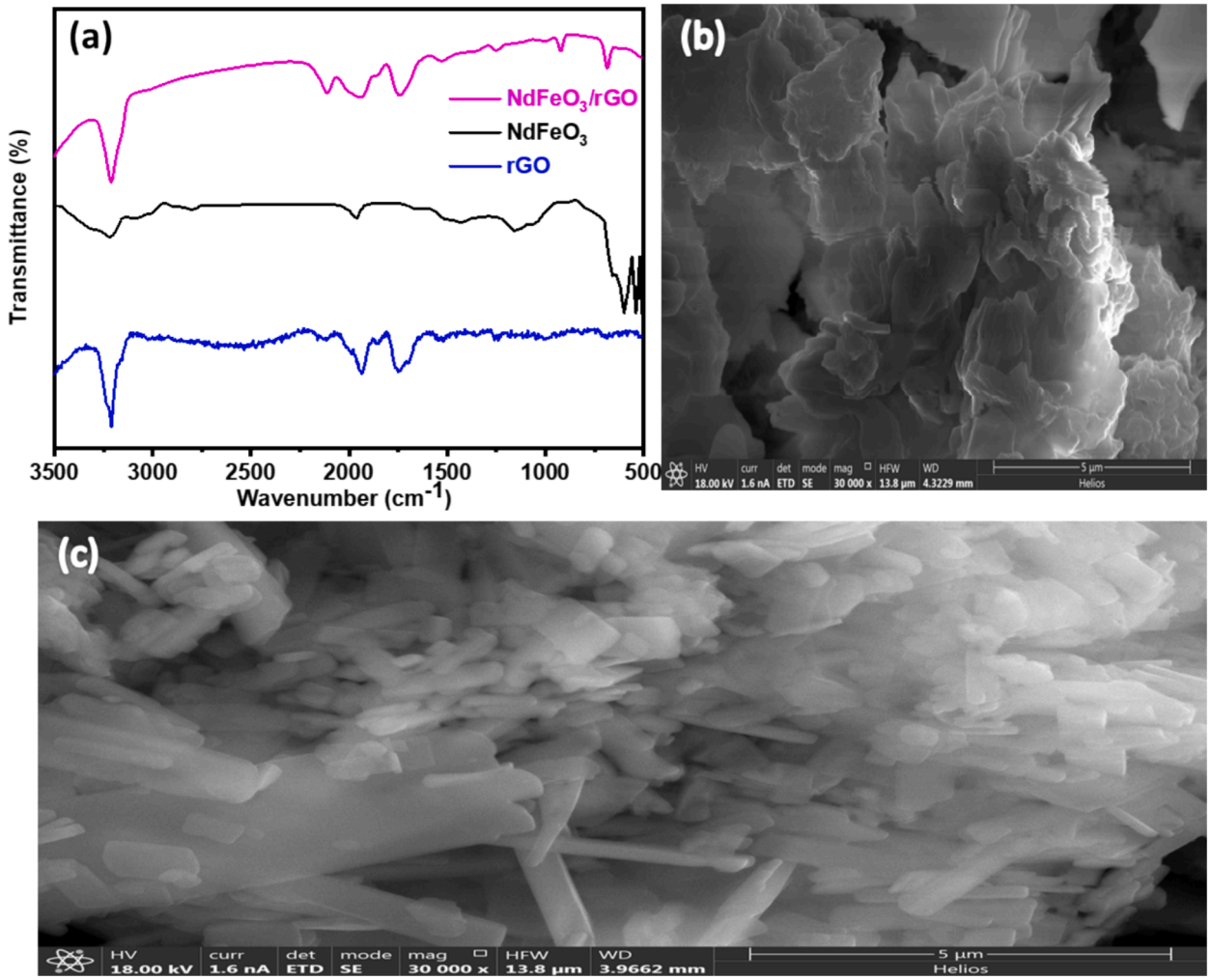

Fig. 2. (a) Comparison of FTIR spectrum for $NdFeO_3$, rGO and $NdFeO_3$/rGO, (b) SEM images for rGO, and (c) $NdFeO_3$ nanorods.

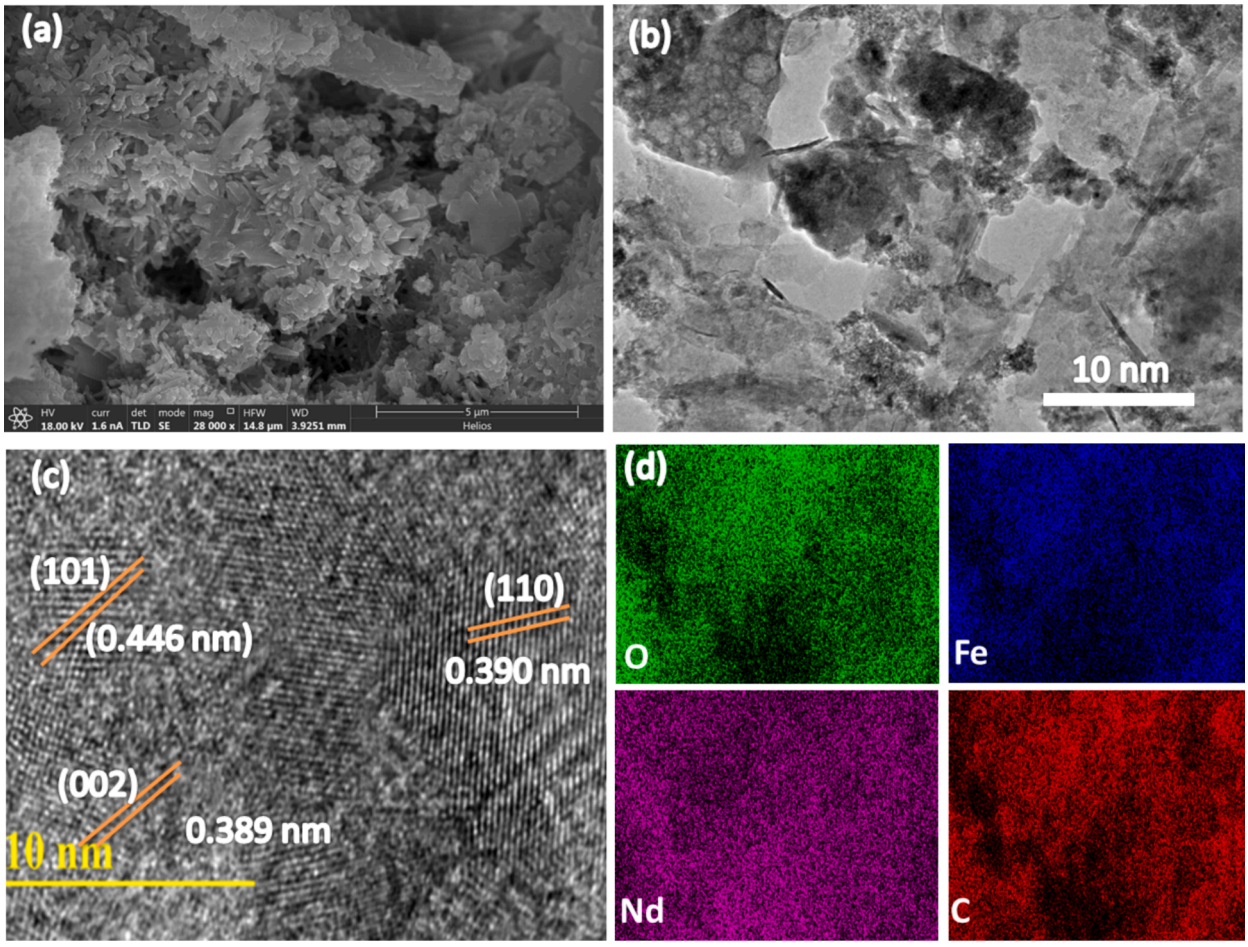

Fig. 3. (a) SEM analysis for the $NdFeO_3$/rGO, (b) TEM image at low and high magnifications, (c) HRTEM analysis, and (d) elemental mapping for the nanocomposite.

the layers of graphene structures. Besides, HR-TEM image in Fig. 3c indicated the well-developed lattice fringes of $NdFeO_3$. Elemental mapping was used to perform elemental analysis, which confirmed the purity of the produced $NdFeO_3$/rGO, as shown in Fig. 3d. It also indicated the presence of relative elements like Nd, Fe, O, and C in $NdFeO_3$/rGO.

In addition, the surface elements in the neodymium ferrite were analyzed using XPS to determine their chemical state and composition. From the XPS spectrum shown in Fig. 4a, it can be noticed the presence of Nd, Fe, O, and C elements at the surface of the material. Fe 2p3/2 XPS spectra showed peaks that corresponded to Fe^{3+} ions in the oxide state, with binding energies of 706 eV [42] and 710.6Ev [35]. Additionally, there was a another peak at 724.3 eV [43], suggesting the presence of both Fe^{2+} and Fe^{3+} states. Based on the XPS analysis, it was determined that the majority of iron exists in the Fe^{3+} states shown in Fig. 4d. 3d spectrum (Fig. 4c) related to Nd provided two spin–orbit features, representing the Nd 3d3/2 and Nd 3d5/2 components, observed at specific binding energy (BE) values 1003.4 [38] and 980.4 eV [39], respectively. This suggests the presence of Nd in the Nd^{3+} oxidation state, similar to what a materials scientist would observe. Through peak fitting, two unique peaks were recorded at binding energies of 980.4 [39] and 979.24 eV[39]. These peaks can be attributed to the presence of Nd_2O_3 and the transfer of electrons from oxygen to Nd 4f3. Fig. 4d shows the O 1 s feature, which appeared at 529.3 eV [16]. It can be broken down into peaks at 529.03 and 531.43 eV [44], indicating Nd-O and Fe-O bonding and surface hydroxyl species, respectively. X-ray photoelectron spectroscopy (XPS) analysis of the C1s (Fig. 4e) peak in reduced graphene oxide (rGO) consists of multiple peaks corresponding to different carbon species, including sp2-hybridized carbon atoms in graphitic domains and various functional groups such as hydroxyl (–OH), epoxy (−O), carbonyl (>C═O), and carboxyl (–COOH) groups. The main peak in the C1s spectrum typically arises from sp2-hybridized carbon atoms in the graphitic lattice, appearing at a binding energy around 284.5 eV [45]. This peak represents the π-π* transition of carbon atoms in aromatic rings, characteristic of graphene-like structures in rGO. Additional peaks may appear at higher binding energies, corresponding to oxygen-containing functional groups. These peaks typically occur at binding energies higher than 284.6 eV[33] due to the electron-withdrawing effects of oxygen atoms. a dominant peak at 285.5 eV [46] indicates a more graphene-like structure with fewer oxygen-containing functional groups.

3.2. Electrochemical oxygen evolution reaction

The Electrochemical OER is assessed by using three electrode setups, in which prepared NF is used as working electrode, Pt wire as counter electrode and Ag/AgCl as reference electrode. The applied potential is converted to Reversible hydrogen electrode (RHE) by using the above-mentioned equation (1). IR correction is applied to obtained LSV data. The LSV curve obtained at a scan rate of 10 mVs^{-1} in 1 M KOH electrolyte is shown in Fig. 5a. It is evident that all samples achieve the pre-oxidation peak at 1.35 V vs RHE prior to the start of OER, which may be caused by the oxidation of Fe and Nd ions to their higher valence states. The LSV scans showed that the defective perovskite $NdFeO_3$@rGO (1.4 V) had a lower onset potential than rGO (1.5 V) and $NdFeO_3$ (1.54 V). The $NdFeO_3$@rGO achieve higher current density of 100, 500, and 1000 $mAcm^{-2}$ with an overpotential of 220, 255, and 345 mV, respectively, compared to $NdFeO_3$(100 $mAcm^{-2}$ at 330 mV), and rGO (100 $mAcm^{-2}$

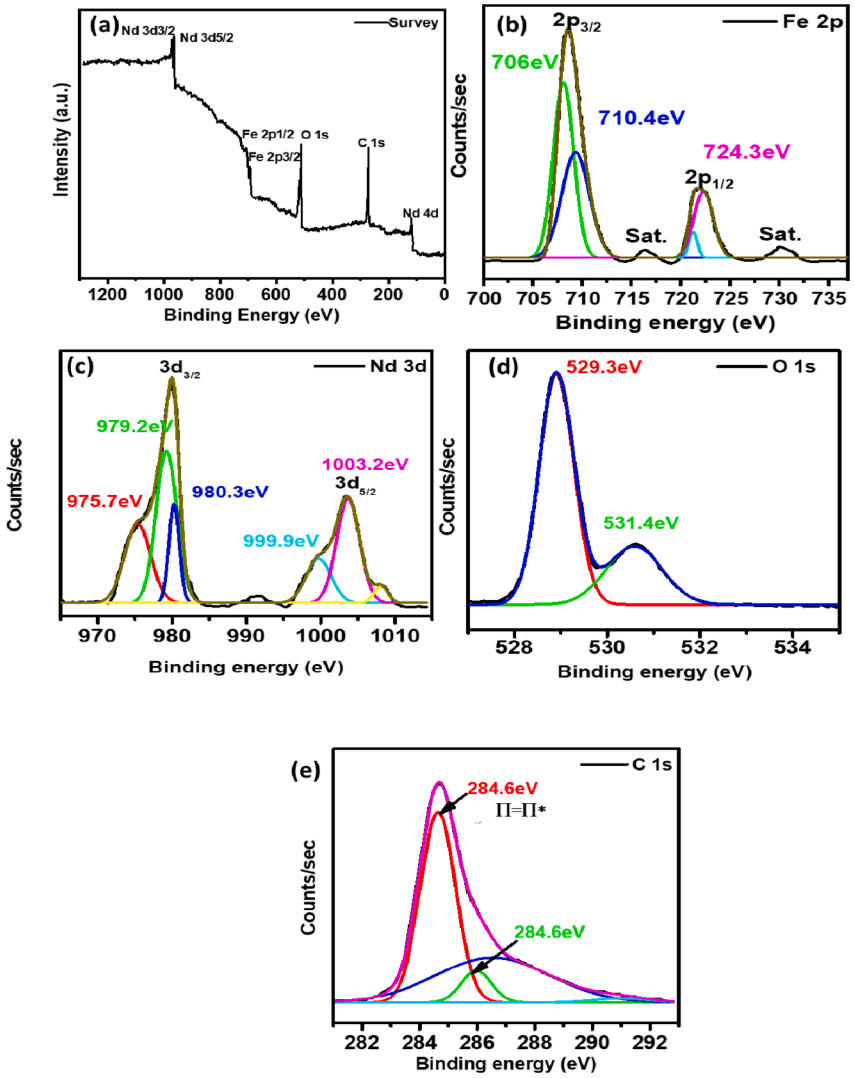

Fig. 4. Comparison of XPS spectrum for $NdFeO_3$@rGO (a) Survey spectrum (b) Fe 2p (c) Nd 3d (d) O1s (e) C1s.

at 290 mV). These results surpass those of OER electrocatalysts (Table 2).

In Fig. 5b, we can observe that the Tafel slope analysis sheds light on the electrocatalytic properties of $NdFeO_3$@rGO and $NdFeO_3$, obtained by plotting the straight-line graph of logj vs overpotentials. Different materials display unique properties in the Tafel slopes, which are used to quantify the rate of electrochemical reaction. The comparison of OER activity is shown comparing the Tafel slope of rGO, $NdFeO_3$ and $NdFeO_3$/rGO. Among prepared samples, the smaller value of tafel slope is shown by composite material 34 mV/dec. Contrarily, the $NdFeO_3$ and rGO depicts the 89 mV/dec and 106 mV/dec respectively which suggest that the $NdFeO_3$/rGO have faster kinetics of OER as compared to $NdFeO_3$ and rGO. The integration of $NdFeO_3$ with rGO results in a synergistic effect, as this significant decrease in Tafel slope suggests accelerated electrical potential and faster kinetics for OER. It is well documented that the performance of renewable energy electrocatalysts is determined by their structure and material composition. In present case the oxygen vacancies and defects provide immense boost to OER. As it is previously reported that adsorption of water molecules (H_2O) requires defect sites, particularly oxygen vacancies. OER may arise in lattice flaws. Water molecules oxidize at these vacancies during adsorption, forming •OH radicals. Hydroxyl radicals then oxidize to generate oxygen molecules (O_2), releasing protons (H^+) and electrons. Sustainable energy conversion materials' catalytic efficacy depends on defect engineering and surface chemistry, and causing oxygen vacancies, which are crucial to water oxidation and oxygen evolution.

In order to understand how $NdFeO_3$, rGO, and the $NdFeO_3$@rGO composite perform electrochemically OER mechanism, it is necessary to perform an impedance spectroscopy analysis shown in Fig. 5c. Polarization resistance (Rp) measures that researchers use to assess the materials' conductivity and the rate of charge transfer. In case of $NdFeO_3$ the Polarization resistance (Rp) = 340.3 O, suggesting difficulty in transferring charges at the interface between the electrode and electrolyte when conducting OER. Surface imperfections, low electrical conductivity, or a lack of active catalytic sites could all contribute to $NdFeO_3$ unusually high polarization resistance, which in turn suggests slower kinetics for the OER. While the rGO shows the polarization resistance (Rp) to be 294 O. It is clearly evident that higher values of Rp impacting catalytic activity and conductivity which describes slower kinetics of OER for rGO and $NdFeO_3$. The composite $NdFeO_3$@rGO, on the other hand, has a polarization resistance (Rp) of only 14.4 O, indicating the smooth charge transfers across the electrolyte–electrode interface during OER as shown in Fig. 5 c. It appears that the $NdFeO_3$ and rGO phases in the composite work together to improve polarization resistance, which in turn improves the conductivity and catalytic activity. Similarly, the composite has a small value of solution resistance (Rs) of 2.3 O, that also suggest that the prepared electrocatalyst is completely feasible to perform remarkable OER activity.

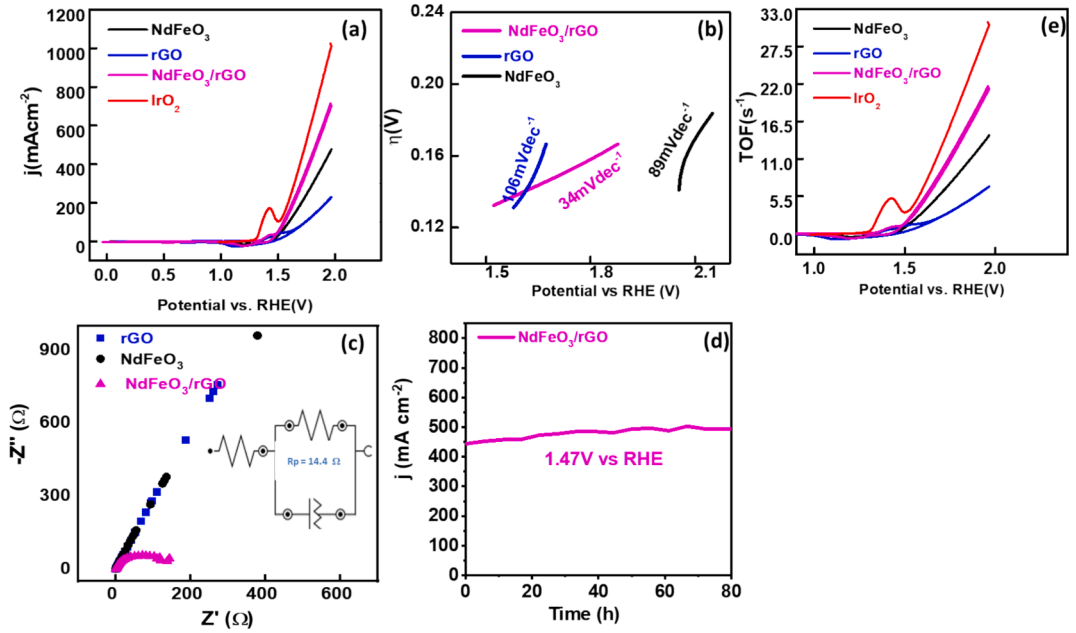

Fig. 5. Comparison of electrochemical OER test for $NdFeO_3$, rGO and $NdFeO_3$/rGO (a) LSV curve, (b) Tafel slope analysis, (c) Impedance spectrum (inset EIS circuit), (d) Chronoamperometry test, and (e) TOF of all the synthesized products.

Table 2
Comparison of OER acitivity of $NdFeO_3$, rGO and $NdFeO_3$/rGO.

Sample	Onset potential (V)	$\eta^{-2}_{100mAcm}$ (mV)	$H^{-2}_{500mAcm}$ (mV)	$H^{-2}_{1000mAcm}$ (mV)	Tafel value (mV dec^{-1})	Rct (Ω)
$NdFeO_3$	1.54	330	––	––	89	340.3
RGO	1.5	293	338	539	106	298.4
$NdFeO_3$/rGO	1.40	220	255	345	34	14.4
IrO_2	1.46	210	340	355	46	2.2

In $NdFeO_3$/rGO, the key components that galvanize HER and OER are the transition metal (Fe) sites in the $NdFeO_3$ lattice and the synergistic interaction between $NdFeO_3$ and rGO. Particularly when reduced or partly oxidized, the Fe sites are often active sites for hydrogen adsorption and subsequent development in HER. Adding more active sites to rGO may increase catalytic activity. It also enhances the composite's conductivity, which simplifies electron transport. The Nd ion presumably helps to stabilize the reaction intermediates, and the Fe sites in $NdFeO_3$, which change oxidation state during the process, are important catalytic centers for OER. The rGO decreases overpotentials in both HER and OER, improving total charge transfer. Furthermore, the interaction between rGO with $NdFeO_3$ may modify the system's electronic structure, enhancing the adsorption energies of reaction intermediates and overall catalytic efficiency. The propose of the unit cell structure of NdFeO3/rGO is pivotal to comprehending its influences in water splitting. On the other hand, $NdFeO_3$ possesses a cubic symmetry (Fig. 1b). Notably, the presence of oxygen defects in perovskite structures, such as $NdFeO_3$, which appeared through synergy of rGO and $NdFeO_3$ significantly impacts their electrocatalytic performance. The tolerance factor and the Jahn-Teller effect both play crucial roles in shaping the crystal structure and properties of crystal structure which in turn influence its electrocatalytic behavior. The tolerance factor (t) determines the compatibility of the A-site and B-site cations within the perovskite lattice. When t approaches unity, $NdFeO_3$ adopts an ideal cubic perovskite structure, minimizing structural distortions. Deviations from unity can lead to distortions that create additional active sites for catalytic reactions or alter the electronic structure, affecting electrocatalytic performance. The departure from unity of the low tolerance factor, in $NdFeO_3$/rGO is attributed to the relatively large ion radius of Nd^{3+} compared to Nd^{2+}, leading to structural deformation The ionic radii of the constituent ions Nd^{3+} (1.08 Å), O^{2-} (1.4 Å), and Fe^{3+} (0.645 Å) play a crucial role in the bonding characteristics within the composite structure. While this effect comes from degenerate orbitals of Fe^{3+} and Nd^{3+} ions. It can produce various defects by creating distortions altering the material electronic properties. In order to understand the reason for such remarkable electrochemical performance of $NdFeO_3$/rGO is critical to comprehend the jahn teller effect and tolerance factor. With an enhancement in the number of active sites and facilitation of charge migration, rGO invigorates the electrocatalytic performance of $NdFeO_3$ and increases its overall catalytic efficiency. Its large surface area and conductivity further contribute to this improvement [47].

$$t = (rA + rB)/\sqrt{2}(rB + rO)$$

The stability of the $NdFeO_3$/rGO electrocatalyst was evaluated by chronoamperometry. Fig. 5d shows the stability test required a long duration, about 80 h, of applying a steady voltage of 1.75 V vs RHE. Surprisingly, the $NdFeO_3$/rGO composite performed quite well under these conditions, showing no significant degradation. The chronoamperometry tests showed that the OER currents were stable and consistent throughout the testing period, which means that the composite performed well and remained stable over time at the applied potential of 1.75 V vs RHE. This remarkable stability guarantees dependable and long-lasting performance over long periods of operation, which is crucial for practical applications in electrochemical water splitting. A sustainable energy conversion technology could benefit from the $NdFeO_3$/rGO composite's capacity to keep its catalytic activity intact even when subjected to long-term OER conditions. Furthermore, the TOF was also calculated to check the activity of the fabricated samples. The TOF of the $NdFeO_3$@rGO was good as compared to the individuals like $NdFeO_3$, rGO, as well indicating the good OER activity as shown in

Fig. 7e.

Another important parameter is the surface area analysis using electrochemical methods, which was conducted to record ECSA of $NdFeO_3$ and $NdFeO_3$/rGO. ECSA is calculated by using double layer capacitance which is obtained by plotting linear region of change in current density at various scan rates. The comparison of CV curves in non-faradic region is demonstrated in Fig. 6 (a–c). The comparison of Cdl values for $NdFeO_3$, rGO and $NdFeO_3$/rGO in Fig. 6d suggest that the ECSA value increases considerably for composite $NdFeO_3$/rGO (17 $mFcm^{-2}$) as compared to the $NdFeO_3$ (11 $mFcm^{-2}$) and rGO (3.2 $mFcm^{-2}$). It is previously reported that larger ECSA, will higher be the available number of active sites used to carry out electrocatalytic surface reactions. The raised ECSA may be devoted to the various defects generated within the $NdFeO_3$/rGO and alteration occurred in the crystal lattice of $NdFeO_3$ after dispersing on the surface of rGO sheets. These findings highlight capability of the prepared composite $NdFeO_3$/rGO is most favorable and pragmatic electrocatalyst, displays numerous active sites, critical for increasing OER and HER activity in vast applications of electrochemical devices.

3.3. Electrochemical HER activity in 1 M KOH solution

The prepared electrocatalysts have been tested for HER activity in 1 M KOH solution. We obtained HER currents at room temperature by using linear sweep voltammetry (LSV) with a scan rate of 10 mV/s at voltage scanned from 0 to −2 V vs Ag/AgCl. Fig. 7a displays the modified iR LSV values for $NdFeO_3$, rGO and $NdFeO_3$/rGO. The $NdFeO_3$/rGO nanocomposite exhibited onset currents of 0.116 V for negative scans. This indicates a reduced overpotential compared to $NdFeO_3$ (0.312 V) and rGO (0.246 V). Exceeding the performance of extremely active HER catalysts such as Pt (about 0.50 V). The $NdFeO_3$/rGO array outperformed the individual $NdFeO_3$ and rGO, achieving higher current densities of 100, 500, and 1000 $mAcm^{-2}$ at overpotentials of 206, 301, and 466 mV, respectively. In comparison, $NdFeO_3$ and rGO exhibited only current densities of 100 $mAcm^{-2}$, at overpotential of 665 mV and 256 mV respectively, at elevated overpotentials, as seen in Table 3..

Fig. 7b displays the Tafel plot of HER regarding the average capacitance- and iR-corrected linear sweep voltammograms (LSVs) of $NdFeO_3$, rGO, and $NdFeO_3$/rGO. The obtained Tafel slopes of 175 mV dec^{-1} for $NdFeO_3$ and 93 mV dec^{-1} for rGO. The Tafel slope analyses indicate that perovskite composite $NdFeO_3$/rGO (47 mV dec^{-1}) exhibits rapid HER activity than perovskite $NdFeO_3$ and rGO across all potential ranges. There is an increasing difference in the amount of activity between the two oxides at high potentials. Impedance spectroscopy offers useful insights into the electrochemical behavior and performance of $NdFeO_3$, rGO, and their composite $NdFeO_3$@rGO in HER depicted in Fig. 7c. The results were superior to those of previously documented state-of-the-art HER electrocatalysts (Table 4). Furthermore, the researchers can evaluate the charge transfer kinetics and overall conductivity of materials by measuring the polarization resistance (Rp) and solution resistance (Rs) as calculated via fitted data as depicted in Fig. 7d. Polarization resistance refers to the resistance to charge transfer at the electrode–electrolyte contact. The impedance spectra of $NdFeO_3$ show a polarization resistance (Rp) of 413 O and a solution resistance (Rs) of 4.09 O during the hydrogen evolution reaction (HER). A higher value indicates slower kinetics for hydrogen evolution in $NdFeO_3$. Impedance spectroscopy studies on rGO show a polarization resistance (Rp) of 37.5 Kohms and a solution resistance (Rs) of 1.70 O. A higher polarization resistance indicates slower charge transfer kinetics. On the other hand, the composite $NdFeO_3$@rGO has a substantially lower polarization resistance (Rp) of 468 m ohms, indicating enhanced charge transfer kinetics during the hydrogen evolution reaction (HER). Furthermore, the composite's solution resistance (Rs) was found to be 1.65 O, indicating that its conductivity is comparable to that of the individual components as depicted in Fig. 7(e–g). On the other hand, the TOF is also an important parameter to check the activity of the fabricated samples like $NdFeO_3$, rGO, and $NdFeO_3$@rGO. The TOF of the

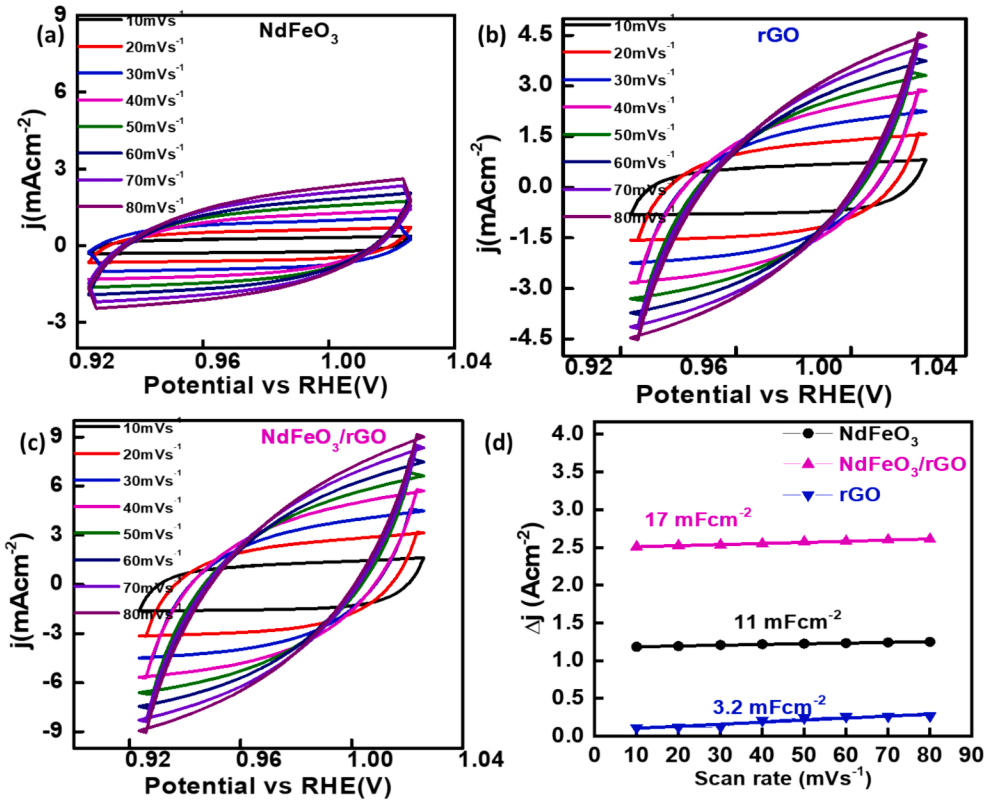

Fig. 6. Comparison of CV curve obtained under non-faradic region (a) $NdFeO_3$, (b) rGO and (c) $NdFeO_3$/rGO (d) linear region plot.

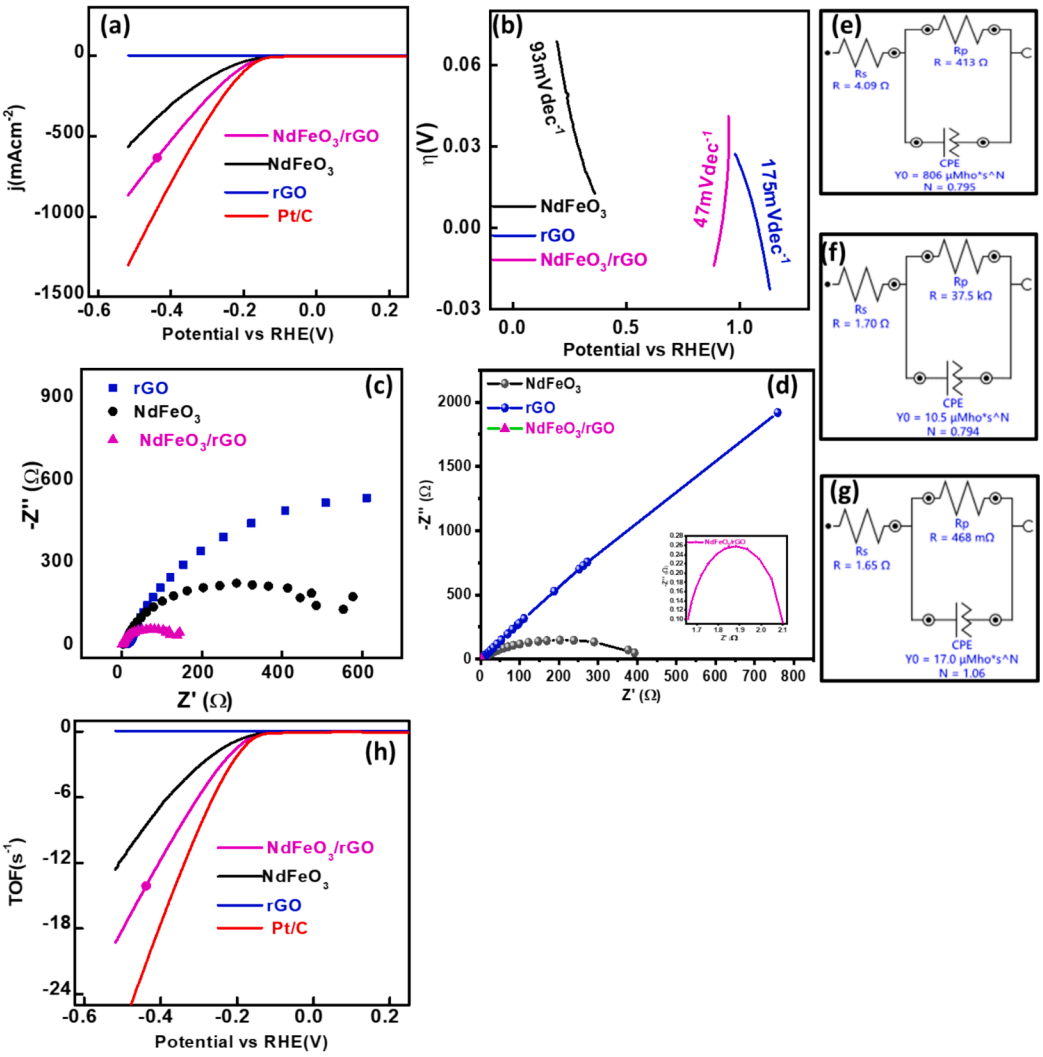

Fig. 7. Comparison of electrochemical HER test for $NdFeO_3$, rGO and $NdFeO_3$/rGO (a) LSV curve (b) Tafel slope analysis (c) Impedance spectrum, and (d) EIS fitted spectrum, (e-g) EIS fitted circuit for NdFeO3, rGO, and $NdFeO_3$/rGO, and (h) TOF of all the synthesized products.

Table 3
Comparison of $NdFeO_3$, rGO, and the $NdFeO_3$@rGO for HER activity.

Sample	Onset potential (V)	$\eta^{-2}_{100mAcm}$ (mV)	$\eta^{-2}_{400mAcm}$ (mV)	$H^{-2}_{1000mAcm}$ (mV)	Tafel value (mV/dec)	Rct (Ω)
$NdFeO_3$	0.312	665	––	–—	175	352
rGO	0.246	256	––	––	93	214.4
$NdFeO_3$/rGO	0.116	206	301	466	47	13.3
Pt/C	0.044	100	198	355	46	2.3

Table 4
Comparison of electrocatalyst with previously reported literature.

Sample	η at 10 $mAcm^{-2}$	Tafel slope (mV dec^{-1})	Electrochemical activity	References
$BaZr_xFe_{1-x}O_{3-\delta}$	324	–-	OER	[21]
$CaCu_3Ti_4O_{12}$	333	48	OER	[48]
$PrBaCo_2O_{5.5}$	245	89	OER	[49]
P-3G	372	45	OER	[50]
$SmFeO_3$/rGO	180	34	OER	[46]
N-$Sr_2Fe_{1.5}Mo_{0.5}O_{6-\delta}$	253	59	HER	[12]
$(PrSr)_3(FeNb)_2O_7$	124	45	HER	[12]
$LaFeO_3$-RGO	120		HER	[25]
L-0.5/rGO	145	–-	HER	[31]

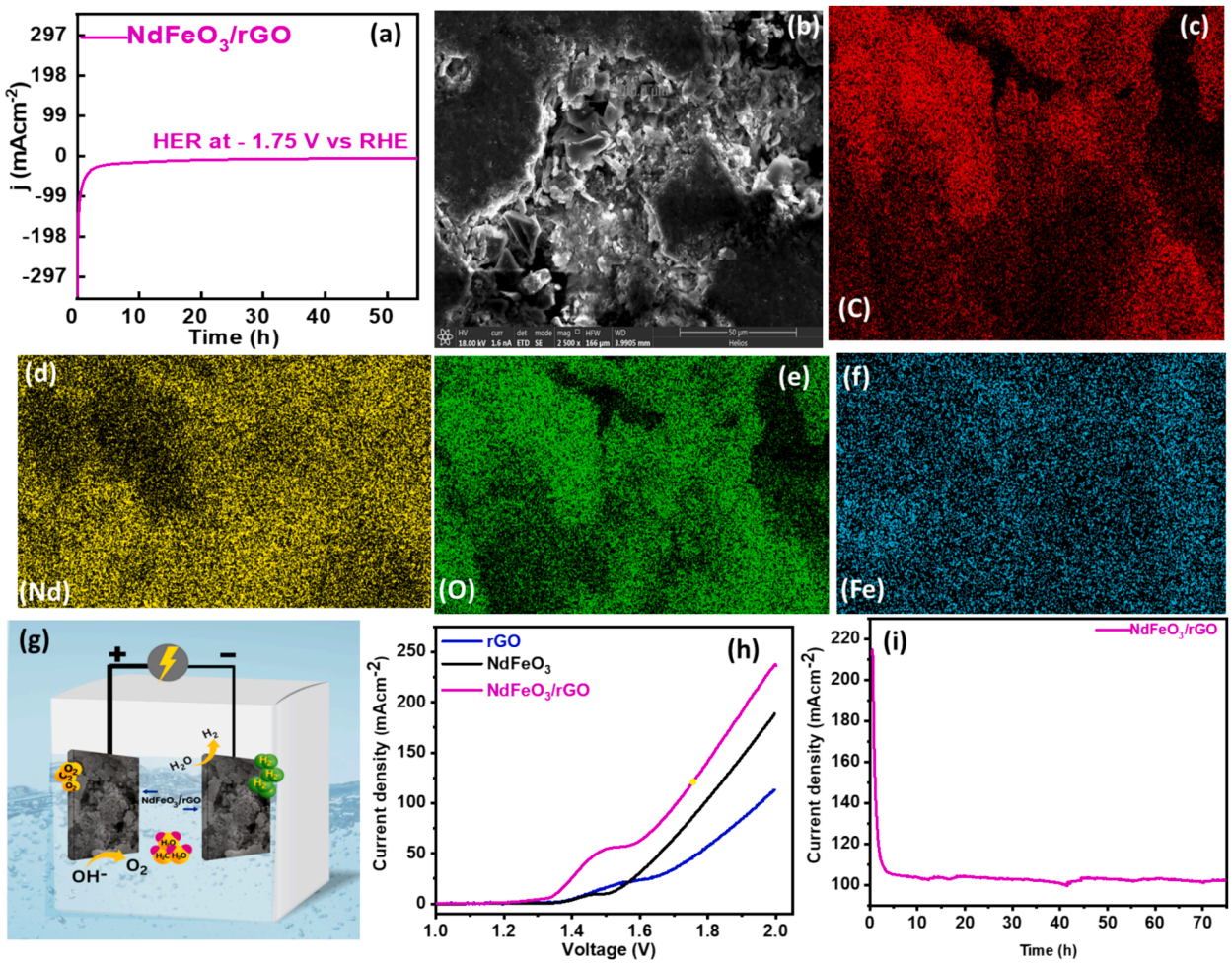

Fig. 8. (a) Chronoamperometry of the nanocomposite, (b) FESEM of the nanocomposite after stability test, (c-f) elemental mapping for the nanocomposite to confirm the presence of elements.

nanocomposite was good as compared to the individuals as well indicating the good HER activity as shown in Fig. 7h.

During the chronoamperometry investigation, the stability of the $NdFeO_3$@rGO composite for HER was determined. Fig. 8a shows that a constant applied potential of −1.75 V vs RHE was given and capable of sustain the current density of -60 $mAcm^{-2}$ for about 55 h without any considerable downfall. It indicates its robustness and durability of electrocatalyst for energy conversion devices. This prominent its significant potential for practical application in electrochemical water splitting and hydrogen production. On the other hand, to check the morphological stability of the resultant material we have performed the FE-SEM as shown in Fig. 8b, indicating that the materials retain its morphology well and some of the agglomerated particles were due to the presence of many hydroxyl ions on the surface of the catalyst. Furthermore, to check the elemental composition after stability of 55 h, the elemental mapping was performed and were shown in Fig. 8(c–f). The resultant material indicates the relative elements of the nanocomposite also indicating the stability of the fabricated materials as well. A two-electrode system electrolysed with 1.0 M KOH using $NdFeO_3$, rGO, and $NdFeO_3$/rGO as the cathodic and anode electrodes is shown in Fig. 8g. The linear sweep voltammetry curve, which was done at a scan rate of 10 mVs^{-1}, is shown in Fig. 8h. The LSV curve indicates that the generated electrocatalyst may catalyse OER and HER by splitting a water molecule at low overpotentials. At 1.35, 1.50, and 1.45 V for $NdFeO_3$/rGO, $NdFeO_3$, and rGO, respectively at a current density was 10 $mAcm^{-2}$, Additionally, the chronoamperometry approach is employed to evaluate the produced electrocatalyst for long-term OER and HER activity. The $NdFeO_3$/rGO electrocatalyst may remain active for more than 70 h with very minor fluctuations in current density, as illustrated in Fig. 8i. This gives more proof of the electrodes' resilience. The extraordinary activity of the produced electrocatalyst for OER and HER makes it suitable for low-cost energy conversion and storage devices, as well as commercial-scale applications.

The remarkable OER and HER activity of $NdFeO_3$@rGO composite can be ascribed to the synergism produced after forming composite of $NdFeO_3$@rGO which provide myriad active sites and augment the polarization of charges across the interphase. This composite offers dense and robust framework thus having intrinsic activity This synergy increases the number of active sites density of active sites, as well as it produces uniformly distributed active sites, resulting in higher catalytic efficiency. The high electrical conductivity of rGO contributes significantly to efficient charge transport inside the composite. The increased conductivity allows electrons to travel swiftly and effectively through the material, lowering the overpotential required for certain processes and resulting in quicker reaction kinetics. The lattice structure of $NdFeO_3$ when form composite with rGO greatly influences its unit cell composition by varying its ionic radius and cell volume, which is tuned owing to the synergism generated in the composite $NdFeO_3$/rGO. These defects and change in electronic structures are evident by tolerance factor and Jahn teller effect, basing the material remarkable performance for the water splitting reactions. The deviation in tolerance factor suggest that distortion might have happened in the crystal lattice of $NdFeO_3$/rGO. Moreover, the conductivity of $NdFeO_3$/rGO evident in Impedance spectrum further supports that the electrocatalyst have

intrinsic capability t perform OER and HER in alkaline media. These features make this electrocatalyst an ideal option to carry out energy conversion devices.

4. Conclusion

This paper underwent a complete investigation of structural, morphological, elemental and electrochemical activity of $NdFeO_3$/rGO, $NdFeO_3$ and rGO. The nanoparticles of $NdFeO_3$/rGO have been synthesized by using ultrasonic method at low temperature. Nearly homogeneous nanorods of $NdFeO_3$ are found uniformly distributed over the nanosheets of rGO. For OER, $NdFeO_3$/rGO possessed lower overpotentials of 255 and 345 mV at current densities of 500 and 1000 $mAcm^{-2}$ respectively. Notably, $NdFeO_3$/rGO exhibited prolonged testing for yielding O_2 gas bubbles for 60 h during chronoamperometry. In case of HER, it also approaches higher current density of 500 $mAcm^{-2}$ and 1000 $mAcm^{-2}$ at 301 mV, and 466 mV overpotential respectively. The robustness of this electrocatalyst for HER depicts its ability for 55 h. The surpassed OER and HER performance of fabricated $NdFeO_3$/rGO can be attributed to the tailored construction, lattice structure, and enhanced conductivity due to the anchoring of rGO. The $NdFeO_3$/rGO proposed insights for fabricating earth-abundant, economical, and environmentally feasible electrocatalysts for various energy devices.

5. Declaration

5.1. Compliance with ethical standards

Yes, this article compliance with ethical standards of journal.
Ethical Approval.

- The manuscript has not been submitted to anyone journal for simultaneous consideration.
- The submitted work is original and should not have been published elsewhere in any form or language (partially or in full) unless the new work concerns an expansion of previous work. (Please provide transparency on the re-use of material to avoid the concerns about text-recycling ('self-plagiarism').
- A single study should not be split up into several parts to increase the quantity of submissions and submitted to various journals or to one journal over time (i.e. 'salami-slicing/publishing').
- Concurrent or secondary publication is sometimes justifiable, provided certain conditions are met. Examples include: translations or a manuscript that is intended for a different group of readers.
- Results should be presented clearly, honestly, and without fabrication, falsification, or inappropriate data manipulation (including image-based manipulation). Authors should adhere to discipline-specific rules for acquiring, selecting and processing data.
- No data, text, or theories by others are presented as if they were the author's own ('plagiarism'). Proper acknowledgements to other works must be given (this includes material that is closely copied (near verbatim), summarized and/or paraphrased), quotation marks (to indicate words taken from another source) are used for verbatim copying of material, and permissions secured for material that is copyrighted.

Funding Declaration
This work was funded by the Researchers Supporting Project Number (RSPD2024R645) King Saud University, Riyadh, Saudi Arabia.

CRediT authorship contribution statement

Khalid A. Alrashidi: Writing – original draft, Methodology, Investigation, Funding acquisition, Formal analysis, Data curation. **Iram Manzoor:** Writing – original draft, Validation, Methodology, Formal analysis, Data curation. **Abdul Ghafoor Abid:** Writing – original draft, Validation, Methodology, Investigation, Formal analysis, Data curation. **Saikh Mohammad:** Writing – original draft, Validation, Resources, Methodology, Investigation, Formal analysis, Data curation. **Muhammad Bilal:** Writing – original draft, Methodology, Investigation, Formal analysis, Data curation. **Nadir Abbas:** Writing – original draft, Validation, Methodology, Investigation, Formal analysis. **Farooq Ahmad:** Writing – original draft, Visualization, Methodology, Investigation, Formal analysis, Data curation. **Jafar Hussain Shah:** Writing – review & editing, Project administration, Conceptualization.

Declaration of competing interest

The authors declare that they have no known competing financial interests or personal relationships that could have appeared to influence the work reported in this paper.

Acknowledgment

This work was funded by the Researchers Supporting Project Number (RSPD2024R645) King Saud University, Riyadh, Saudi Arabia.

References

[1] X. Xu, et al., Electrochemical hydrogen storage materials: state-of-the-art and future perspectives, Energy Fuel 38 (9) (2024) 7579–7613.
[2] K. Li, et al., Anion-modulated CoP electrode as bifunctional electrocatalyst for anion-exchange membrane hydrazine-assisted water electrolyser, Mater. Horiz. 10 (11) (2023) 5277–5287.
[3] W. Huang, et al., Sulfur-Modified Nickel-Based Hybrid Nanosheet as a Robust Bifunctional Electrode for Hydrogen Generation via Formaldehyde Reforming, ACS Appl. Energy Mater. 6 (13) (2023) 7221–7229.
[4] Q. Wang, et al., Engineering of electronic states on Co3O4 ultrathin nanosheets by cation substitution and anion vacancies for oxygen evolution reaction, Small 16 (24) (2020) 2001571.
[5] J. He, et al., Oxygenate-induced structural evolution of high-entropy electrocatalysts for multifunctional alcohol electrooxidation integrated with hydrogen production, Proc. Natl. Acad. Sci. 121 (30) (2024) e2405846121.
[6] H. Wang, X. Cheng, Y. Tong, Coupling of ruthenium with hybrid metal nitrides heterostructure as bifunctional electrocatalyst for water electrolysis, J. Colloid Interface Sci. 629 (2023) 155–164.
[7] Q. Sun, et al., Dual anions engineering on nickel cobalt-based catalyst for optimal hydrogen evolution electrocatalysis, J. Colloid Interface Sci. 589 (2021) 127–134.
[8] K. Jiang, et al., Single platinum atoms embedded in nanoporous cobalt selenide as electrocatalyst for accelerating hydrogen evolution reaction, Nat. Commun. 10 (1) (2019) 1743.
[9] H. Zheng, et al., The heterointerface between Fe1/NC and selenides boosts reversible oxygen electrocatalysis, Adv. Funct. Mater. 33 (40) (2023) 2300815.
[10] X. Ren, Y. Tong, The self-reconstruction of Co-modified bimetallic hydroxysulfide nanosheet arrays for efficient hydrazine assisted water splitting, Int. J. Hydrogen Energy 49 (2024) 489–497.
[11] H. Zheng, et al., Highly Reversible Zn–Air Batteries Enabled by Tuned Valence Electron and Steric Hindrance on Atomic Fe–N4–C Sites, Nano Lett. 24 (15) (2024) 4672–4681.
[12] X. Liu, et al., N doped carbon coated multi-metals nanoparticles decorated perovskite as electrocatalyst for efficient hydrogen evolution reaction, Chem. Eng. J. 399 (2020) 125779.
[13] M.S. Alom, C.C.W. Kananke-Gamage, F. Ramezanipour, Perovskite Oxides as Electrocatalysts for Hydrogen Evolution Reaction. 7 (9) (2022) 7444–7451.
[14] T.X. Nguyen, et al., Advanced High Entropy Perovskite Oxide Electrocatalyst for Oxygen Evolution Reaction, Adv. Funct. Mater. 31 (27) (2021) 2101632.
[15] S. Chandrasekaran, et al., Investigation of improved Bifunctional electrocatalytic HER and OER performances of Lanthanum Molybdate supported Graphene oxide composite in Acidic and Alkaline media, Diam. Relat. Mater. 140 (2023) 110457.
[16] D. Feng, et al., Carbon-encapsulated Co2P/P-modified NiMoO4 hierarchical heterojunction as superior pH-universal electrocatalyst for hydrogen production, J. Colloid Interface Sci. 634 (2023) 693–702.
[17] M. Kumar, T.C. Nagaiah, A multifunctional cobalt iron sulfide electrocatalyst for high performance Zn–air batteries and overall water splitting, J. Mater. Chem. A 10 (9) (2022) 4720–4730.
[18] H. Liu, et al., Cation deficiency design: A simple and efficient strategy for promoting oxygen evolution reaction activity of perovskite electrocatalyst, Electrochim. Acta 259 (2018) 1004–1010.
[19] X. Xu, et al., Toward Enhanced Oxygen Evolution on Perovskite Oxides Synthesized from Different Approaches: A Case Study of Ba0.5Sr0.5Co0.8Fe0.2O3−δ, Electrochim. Acta 219 (2016) 553–559.
[20] M. Zhang, et al., Recent development of perovskite oxide-based electrocatalysts and their applications in low to intermediate temperature electrochemical devices, Mater. Today 49 (2021) 351–377.

[21] K. Zhu, et al., Oxygen evolution reaction over Fe site of BaZrxFe1-xO3-δ perovskite oxides, Electrochim. Acta 241 (2017) 433–439.
[22] J. Wang, Y. Gao, F. Ciucci, Mechanochemical Coupling of MoS2 and Perovskites for Hydrogen Generation, ACS Appl. Energy Mater. 1 (11) (2018) 6409–6416.
[23] X. Liu, et al., Nanofiber-based Sm0.5Sr0.5Co0.2Fe0.8O3-δ/N-MWCNT composites as an efficient bifunctional electrocatalyst towards OER/ORR, Int. J. Hydrogen Energy 48 (41) (2023) 15555–15565.
[24] F. Jin, L. Li, T. He, NdBaCo2/3Fe2/3Cu2/3O5+δ double perovskite as a novel cathode material for CeO2- and LaGaO3-based solid oxide fuel cells, J. Power Sources 273 (2015) 591–599.
[25] A. Galal, et al., An Efficient and Durable Electrocatalyst for Hydrogen Production Based on Earth-Abundant Oxide-Graphene Composite, ChemistrySelect 2 (31) (2017) 10261–10270.
[26] Z. Shan, et al., Hollow dodecahedra graphene oxide-cuprous oxide nanocomposites with effective photocatalytic and bactericidal activity, Front. Chem. 9 (2021) 755836.
[27] B. Xie, et al., Advances in Graphene-Based Electrode for Triboelectric Nanogenerator, Nano-Micro Letters 17 (1) (2025) 17.
[28] C. Wang, et al., 1.82 wt.% Pt/N, P co-doped carbon overwhelms 20 wt.% Pt/C as a high-efficiency electrocatalyst for hydrogen evolution reaction, Nano Res. 10 (1) (2017) 238–246.
[29] C. Lei, et al., Charge Engineering of Mo2C@Defect-Rich N-Doped Carbon Nanosheets for Efficient Electrocatalytic H2 Evolution, Nano-Micro Letters 11 (1) (2019) 45.
[30] J. Hu, et al., Preparation of La1−xCaxMnO3 perovskite–graphene composites as oxygen reduction reaction electrocatalyst in alkaline medium, J. Power Sources 269 (2014) 144–151.
[31] B. Hua, et al., All-In-One Perovskite Catalyst: Smart Controls of Architecture and Composition toward Enhanced Oxygen/Hydrogen Evolution Reactions, Adv. Energy Mater. 7 (20) (2017) 1700666.
[32] C. Han, et al., Catalytic Activity Boosting of Nickel Sulfide toward Oxygen Evolution Reaction via Confined Overdoping Engineering, ACS Appl. Energy Mater. 2 (8) (2019) 5363–5372.
[33] E. Boateng, et al., Tunable Electrochemical Hydrogen Uptake and Release of Nitrogen-Doped Reduced Graphene Oxide Nanosheets Decorated with Pd Nanoparticles, ACS Appl. Nano Mater. 6 (18) (2023) 17311–17323.
[34] G. Chen, et al., Thin NiFeCr-LDHs nanosheets promoted by g-C3N4: A highly active electrocatalyst for oxygen evolution reaction, Nanotechnology 30 (2019).
[35] Q. Ma, et al., Incorporating iron in nickel cobalt layered double hydroxide nanosheet arrays as efficient oxygen evolution electrocatalyst, Electrochim. Acta 317 (2019).
[36] K. Nassar, Solid, Materials for Oxygen Evolution Reaction. (2021).
[37] A. Dobrota, I. Pasti, Chemisorption as the essential step in electrochemical energy conversion - Review, Journal of Electrochemical Science and Engineering 10 (2020).
[38] M. Yousefi, S.S. Zeid, M. Khorasani-Motlagh, Synthesis and characterization of nano-structured perovskite type neodymium orthoferrite NdFeO3, Current Chemistry Letters 6 (2017) 23–30.
[39] B.M. Abu-Zied, A. Khan, Microwave-assisted synthesis of micro/nano NdO powders, J. Mater. Res. Technol. 9 (5) (2020) 10478–10490.
[40] K. Gong, et al., The roles of graphene and its derivatives in perovskite solar cells: A review, Mater. Des. 211 (2021) 110170.
[41] L. Sun, et al., Ultralight and superhydrophobic perfluorooctyltrimethoxysilane modified biomass carbonaceous aerogel for oil-spill remediation, Chem. Eng. Res. Des. 174 (2021) 71–78.
[42] M. Li, et al., Strontium-doped Lanthanum Iron Nickelate Oxide as Highly Efficient Electrocatalysts for Oxygen Evolution Reaction, J. Colloid Interface Sci. 553 (2019).
[43] R. Dumitru, et al., Lanthanum Ferrite Ceramic Powders: Synthesis, Characterization and Electrochemical Detection Application. 13 (9) (2020).
[44] S. Bhowmick, et al., Low Overpotential and Stable Electrocatalytic Oxygen Evolution Reaction Utilizing Doped Perovskite Oxide, La0.7Sr0.3MnO3, Modified by Cobalt Phosphate, ACS Appl. Energy Mater. 3 (2) (2020) 1279–1285.
[45] Y. Zhang, et al., MoS2 and Fe2O3 co-modify g-C3N4 to improve the performance of photocatalytic hydrogen production, Sci. Rep. 12 (1) (2022) 3261.
[46] A. Fatima, et al., Perovskite-type samarium iron oxide adorned on reduced graphene oxide composite: A high-performance electrocatalyst for OER, Diam. Relat. Mater. 145 (2024) 111072.
[47] H. Bourajoini, et al., Calcium manganese oxide catalysts for water oxidation: Unravelling the influence of various synthesis strategies, Mater. Res. Bull. 79 (2016) 133–137.
[48] H.S. Kushwaha, et al., CaCu3Ti4O12: A Bifunctional Perovskite Electrocatalyst for Oxygen Evolution and Reduction Reaction in Alkaline Medium, Electrochim. Acta 252 (2017) 532–540.
[49] Q. Sun, et al., Double perovskite PrBaCo2O5.5: An efficient and stable electrocatalyst for hydrogen evolution reaction, J. Power Sources 427 (2019) 194–200.
[50] Y. Bu, et al., Synergistic interaction of perovskite oxides and N-doped graphene in versatile electrocatalyst, J. Mater. Chem. A 7 (5) (2019) 2048–2054.